Article

Effect of x on the Electrochemical Performance of Two-Layered Cathode Materials xLi_2MnO_3–$(1-x)LiNi_{0.5}Mn_{0.5}O_2$

Renny Nazario-Naveda [1,*], **Segundo Rojas-Flores** [2], **Luisa Juárez-Cortijo** [3], **Moises Gallozzo-Cardenas** [4], **Félix N. Díaz** [2,5], **Luis Angelats-Silva** [6] and **Santiago M. Benites** [1]

1   Vicerrectorado de Investigación, Universidad Autónoma del Perú, Lima 15842, Peru; santiago.benites@autonoma.pe
2   Escuela de Ingeniería Mecánica Eléctrica, Universidad Señor de Sipán, Chiclayo 14000, Peru; segundo.rojas.89@gmail.com (S.R.-F.); diazfelixn@crece.uss.edu.pe (F.N.D.)
3   Grupo de Investigación en Ciencias Aplicadas y Nuevas Tecnologías, Universidad Privada del Norte, Trujillo 13007, Peru; luisa.juarez@upn.edu.pe
4   Facultad de Ciencias de la Salud, Universidad César Vallejo, Trujillo 13001, Peru; mmgallozzo@ucvvirtual.edu.pe
5   Dirección de Gestión Académica, Universidad Tecnológica del Perú, Lima 15419, Peru
6   Laboratorio de Investigación Multidisciplinario, Universidad Privada Antenor Orrego, Trujillo 13008, Peru; langelatss@upao.edu.pe
*   Correspondence: scored731@gmail.com

Abstract: In our study, the cathodic material xLi_2MnO_3–$(1-x)LiNi_{0.5}Mn_{0.5}O_2$ was synthesized by means of the co-precipitation technique. The effect of x (proportion of components Li_2MnO_3 and $LiNi_{0.5}Mn_{0.5}O_2$) on the structural, morphological, and electrochemical performance of the material was evaluated. Materials were structurally characterized using X-ray diffraction (XRD), and the morphological analysis was performed using the scanning electron microscopy (SEM) technique, while charge–discharge curves and differential capacity and impedance spectroscopy (EIS) were used to study the electrochemical behavior. The results confirm the formation of the structures with two phases corresponding to the rhombohedral space group R3m and the monoclinic space group C2/m, which was associated to the components of the layered material. Very dense agglomerations of particles between 10 and 20 μm were also observed. In addition, the increase in the proportion of the $LiNi_{0.5}Mn_{0.5}O_2$ component affected the initial irreversible capacity and the Li_2MnO_3 layer's activation and cycling performance, suggesting an optimal chemical ratio of the material's component layers to ensure high energy density and long-term durability.

Keywords: lithium-ion battery; cathode material; layered composite; Li-rich Mn Ni based

1. Introduction

The world's dependence on fossil fuels is a subject that is still debated today. Although it is true that fossil fuels are necessary for the development of civilization as we know it, it is also important to take into account their impact on the environment [1]. The increase in the demand for energy and the concern for the care of the environment have increased the interest for the use of new energies [2–5]. The use of these energy systems is closely related to the development of increasingly efficient storage systems; hence, much research is focused on improving their performance. The characteristics of lithium batteries, such as their high specific capacity, energy density, and the possibility of using non-toxic reagents in their manufacture [6–9], have enabled them to be used in various technological devices, especially in the automotive area, such as electric vehicles and hybrid electric vehicles [10,11], where energy density plays an important role. In this aspect, lithium batteries surpass other energy storage systems.

Several cathode materials have been used in lithium battery systems [10,12]. Recently, lithium-rich layered oxide (LLO) materials have been considered as promising cathode

materials because of their high capacities (200–300 mAhg^{-1}) with 3.6 V or larger operating voltages when they are charged to over 4.5 V at room temperature [13,14]. Many combinations for these composite materials have been proposed with a general expression such as xLi$_2$MnO$_3$–(1−x)LiMO$_2$ (M = Mn, Ni, Co, Fe, Cr, etc.) [15–19], where excess of Li can be incorporated into the layered structure through the integration of Li$_2$MnO$_3$ in LiMO$_2$, substituting transition metals M [20]. However, LLO materials often show a big decrease in cycling capacity and a low rate capability. These limitations arise because in order for the material to deliver large discharge capacity of more than 200 mAhg^{-1}, it is necessary that cathode be charged above 4.5 V versus Li/Li$^+$ [21,22]. To overcome these drawbacks, many authors have used some oxides, among other materials, as cover materials [15,18,19,23,24] or have proposed different synthesis techniques [25,26].

The compatibility of the structure is clearly seen, and Li$_2$MnO$_3$ can be considered as a particular case of LiMO$_2$. Li$_2$MnO$_3$ has a C2/m monoclinic layered structure and can be represented in the normal layered notation as Li[Li$_{1/3}$Mn$_{2/3}$]O$_2$, composed of alternating Li layers and Li/Mn layers and being structurally compatible with LiMO$_2$, but electrochemically inactive. In a xLi$_2$MnO$_3$–(1−x)LiMO$_2$ composite material, Li$_2$MnO$_3$ provides structural stabilization to LiMO$_2$ because of its electrochemical inactivity between 3 and 4 V vs. Li/Li$^+$. However, Li$_2$MnO$_3$ can transform into an active phase by charging at 4.5 V vs. Li/Li$^+$. The charge mechanism at a high voltage plateau has not yet been well-clarified [26–28]. Some authors presented a composition with the integration of Li$_2$MnO$_3$ domains in a LiMO$_2$ matrix [29–31]. They claim that the results show the existence of two different local structures for both layered materials. On the other hand, a homogeneous solid solution of Li$_2$MnO$_3$ and LiMO$_2$ was reported [26,32]. They stated that the XRD results show a superstructure in the transition metal layer with a Li ordering. Despite their claims being well-supported, there appears a problem when the symmetry is considered, and there is a debate whether it is a solid solution with R3m rhombohedral symmetry or a solid solution with C2/m monoclinic symmetry. Researchers are making efforts to clarify the issue of the structure of layered composite materials because it is essential to understand the relationship between a crystal's structure and electrochemical performance. Based on the latest studies on layered oxide materials, the aim of this research was to synthesize high energy density xLi$_2$MnO$_3$–(1−x)LiMn$_{0.5}$Ni$_{0.5}$O$_2$ cathode materials by means of the co-precipitation method and study the effect of the ratio of transition metals on morphological characteristics and electrochemical performance in terms of current density, voltage, capacity, and ionic impedance.

2. Experimental

2.1. Synthesis of Precursor

In this first step 0.2 M of nickel (II) sulphate hexahydrate [NiSO$_4$·6H$_2$O] (Sigma-Aldrich, St. Louis, MI, U.S., 99%) and 0.2 M of manganese (II) sulphate monohydrate [MnSO$_4$·H$_2$O] (Sigma-Aldrich 98%) were separately dissolved in distilled water and then were mixed together for 10 min with constant stirring. This solution is denoted as Solution A. Separately, a solution of 1 M of sodium bicarbonate [NaHCO$_3$] (Sigma-Aldrich 99%) in distilled water was prepared, and this solution is denoted as Solution B. Solution A was slowly added drop by drop into Solution B by constant magnetic stirring with a temperature of 60 °C. The mixed solution was kept at a pH of 8.5 in order to create the precipitate of Ni$_{(1−x)/2}$Mn$_{(1+x)/2}$CO$_3$; this was obtained by adding an ammonium hydroxide solution [NH$_4$OH] (Sigma Aldrich 28–30%) drop by drop. The mixture was left for 12 h at the same temperature with constant magnetic stirring in order to secure the complete precipitation of the Ni and Mn sulphate solutions on the carbonate solution. After that, the mixture was filtered and washed three times with distilled water. The wet powder was dried for 12 h at 100 °C and then grounded with a mortar and pestle to get the nickel manganese carbonate, the final precursor powder. The quantities of NiSO$_4$·6H$_2$O and MnSO$_4$·H$_2$O varied stoichiometrically, depending on the x value of xLi$_2$MnO$_3$–(1−x)LiNi$_{0.5}$Mn$_{0.5}$O$_2$.

2.2. Synthesis of xLi$_2$MnO$_3$–(1−x)LiNi$_{0.5}$Mn$_{0.5}$O$_2$ Powder

Obtained nickel manganese carbonate powder was mixed with a stoichiometric amount of lithium carbonate [Li$_2$CO$_3$] (Strem Chemicals, Newburyport, MA, U.S., 99.999%) and ground using a mortar and pestle. After intense grinding, the mixture was annealed at 950 °C for 12 h, for which a 6″ W × 6″ D × 6″ H Kerr 666 furnace was used. After 12 h, the calcined powder was quenched at room temperature to keep the oxidation states of the transition metals at 4$^+$ and 2$^+$ for Mn and Ni, respectively. The calcined powder was ground again to obtain the xLi$_2$MnO$_3$–(1−x)LiNi$_{0.5}$Mn$_{0.5}$O$_2$ final powder.

2.3. Electrochemical Coin Cell Fabrication

Coin-type cells (CR2032) were assembled in order to evaluate the electrochemical performance. The cathode material was prepared using 80 wt% of xLi$_2$MnO$_3$–(1−x)LiNi$_{0.5}$Mn$_{0.5}$O$_2$ powder, 10 wt% of carbon black, and 10 wt% of polyvinylidene fluoride. A slurry of the mixed powders was made by using N-Methyl-2-Pyrrolidinone, and it was then coated on aluminum foil (Alfa Aesar, Haverhill, MA, U.S., 99.999%) with a thickness of 0.025. The coated aluminum foil was put in a furnace at 100 °C for 12 h and cut in small circles. For the anode, Li foil with a thickness of 0.75 mm (Sigma Aldrich 99.9%) was used, and the separator was a polypropylene membrane (Celgard 2500, Charlotte, NC, U.S.) with a thickness of 25 μm. A standard electrolyte with 1 mol/kg LiPF$_6$ dissolved in ethylene carbonate (EC) and dimethyl carbonate (DMC) in a 1:2 wt ratio was used. The coin cells were assembled inside of an argon-filled MBraun, Stratham, NH, U.S., glove box.

2.4. Characterization Techniques

In this work, a powder structural analysis was carried out using Siemens D5000 X-ray diffractometer, U.S. (XRD) with Cu Kα radiation (1.5405 Å) in the 2θ angle range from 15° to 75° with a step of 0.02°. A scanning electron microscope (SEM) was used to study the morphology of materials, and the analysis was conducted with a JEOL 7600 FESEM, U.S., system interfaced to a Thermo-Electron System Microanalysis Systems. The samples were adhered to the top of the sample holder with double-sided conductive tape; for better resolution, a Au coating was applied. The electrochemical measurements were evaluated with a Gamry Instruments, Warminster, PA, U.S., G/PC14 potentiostat system. The charge–discharge measurements were performed at room temperature at a voltage range of 2.0–4.8 V using selected current density.

3. Results and Discussion

The X-ray diffraction patterns of the xLi$_2$MnO$_3$–(1−x)LiNi$_{0.5}$Mn$_{0.5}$O$_2$ (x = 0.3, 0.5 and 0.7) synthesized materials are presented in Figure 1a. The typical diffraction pattern of this composed material is shown, where most peaks agree well with the R3m space group related to the rhombohedral type structure for LiMO$_2$ (JCPDS# 09-0063) [31]. The low intensity peaks between 20° and 30° show characteristic peaks of the monoclinic phase, with the space group C2/m associated with the layered composite material Li$_2$MnO$_3$ (JCPDS# 84-1634) [32,33]. The XRD patterns confirm the superlattice phase corresponding to Li$_2$MnO$_3$. The patterns became more obvious when the fraction of the Li$_2$MnO$_3$ layered material was incremented in xLi$_2$MnO$_3$–(1−x)LiMO$_2$. The presence of the small peaks (110), (020), (−111), and (021) is related to the existence of the superstructure caused by the reordering of Li and Mn in the main structure, where lithium ions entered into the transition metal layers positions as expected [32]. Furthermore, the presence of the (006) and (012) peaks confirm the successful formation of a crystalline layered structure with no spinal structure, using co-precipitation synthesis method for all values of x [34,35]. It is clear then that the two structural components of this layered composite prove the coexistence of two compatible phases.
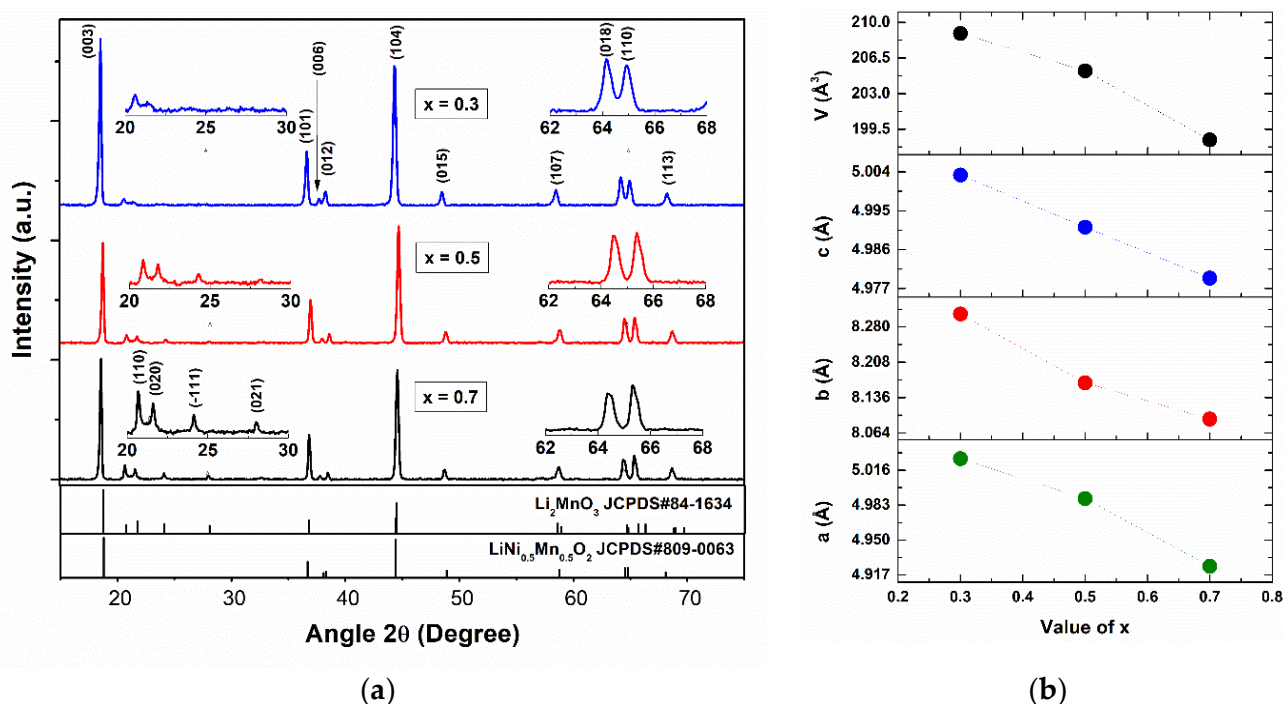
Figure 1. (**a**) X-ray diffraction patterns and (**b**) monoclinic structure lattice parameters of xLi_2MnO_3–$(1-x)LiNi_{0.5}Mn_{0.5}O_2$.

Figure 1b shows the unit cell parameters calculated for all the synthesized materials, based on a monoclinic structure belonging to the C2/m spaces group. The lattice parameters a, b, and c decreased with the x value, specifically with the reduction of Ni in the stoichiometric equation, which corresponded to the increase of the Li content. The stoichiometric ratio of the components' materials was determined when the formula was expressed as $Li[Li_yMn_{1-y-z}Ni_z]O_2$, where $y = x/(2 + x)$ and $z = (1 − x)/(2.5)$. This is shown in Table 1. These decreases in the lattice parameters may be related to both the distribution of lithium ions in the metal layers changing the characteristic order with Mn and the substitution of Mn by Ni [30–33]. Figure 2 shows the crystal structures of layered Li_2MnO_3 and $LiMO_2$, where the compatibility of the structure is clearly seen. Li_2MnO_3 can be considered a particular case of $LiMO_2$, as it is described when it is expressed in layered notation. Additionally, the average size of the crystallite obtained using the Scherrer equation from the diffraction peaks (003) indicated that by means of the co-precipitation method used, nanocrystals at 36.0 nm, 37.8 nm, and 43.9 nm can be obtained for the x values of 0.3, 0.5, and 0.7 respectively.

Table 1. Stoichiometry of Li-rich layered oxides in the most common formulations.

Value of x	xLi_2MnO_3–$(1-x)LiMn_{0.5}Ni_{0.5}O_2$	$Li[Li_yMn_{1-y-z}Ni_z]O_2$
0.3	$0.3Li_2MnO_3$–$0.7LiNi_{0.5}Mn_{0.5}O_2$	$Li[Li_{0.13}Mn_{0.59}Ni_{0.28}]O_2$
0.5	$0.5Li_2MnO_3$–$0.5LiNi_{0.5}Mn_{0.5}O_2$	$Li[Li_{0.20}Mn_{0.60}Ni_{0.20}]O_2$
0.7	$0.7Li_2MnO_3$–$0.3LiNi_{0.5}Mn_{0.5}O_2$	$Li[Li_{0.26}Mn_{0.62}Ni_{0.12}]O_2$

Scanning electron microscopy (SEM) was used to verify the morphology and topology of the synthesized material in order to find some relation between its features and the after-studied electrochemical behavior. As previously explained, the precursor material nickel manganese carbonate $Ni_{(1-x)/2}Mn_{(1+x)/2}CO_3$ had to be previous synthesized. Figure 3 shows the SEM micrographs of the as-synthesized powders of (a) $Ni_{0.35}Mn_{0.65}CO_3$, (b) $Ni_{0.25}Mn_{0.75}CO_3$, and (c) $Ni_{0.15}Mn_{0.85}CO_3$. With a zoom of x5000, it was possible to observe a nearly sphere-like morphology with a uniform particle distribution, similar to

that found by other authors [33,36,37]. Figure 3 shows the precursors' present forms of nearly spherical solids; however, these reduced their size with the increase of Li and Mn (increase in the value of x). In Figure 3a, the agglomerations are larger and less spherical. In addition, small pores and a rougher surface can be observed, likely due to the release of CO_2 in the heat treatment process and the subsequent formation of oxides [38]. Figure 3c shows agglomerations similar to those mentioned above but smaller, with inhomogeneous growth and the presence of some impurities in some parts, associated with the greater formation of MnO_2 [33]. For x = 0.5 (Figure 3b), the agglomerations presented more compact spheres with smooth particles, no pores, and reduced impurities. Figure 4 shows the EDS spectra of precursor materials, confirming the purity of the sample and the absence of additional elements. The intensity represents the proportions of the materials used to make the precursor materials. Ni decreased with x increasing, according to the stoichiometric equation. However, the presence of oxygen was high for x = 0.3, which would explain the presence of the CO_2 formation that decreases as x increases, as shown in the SEM images.
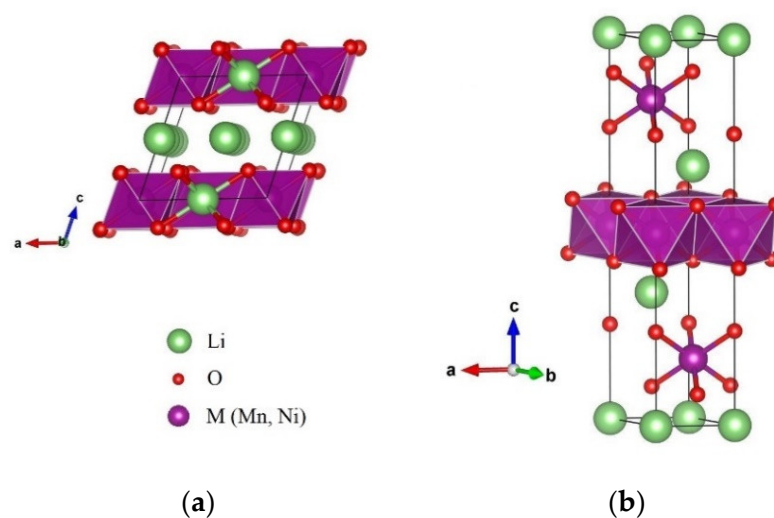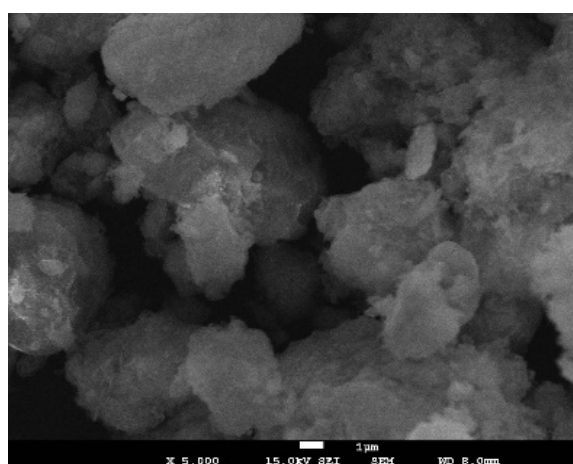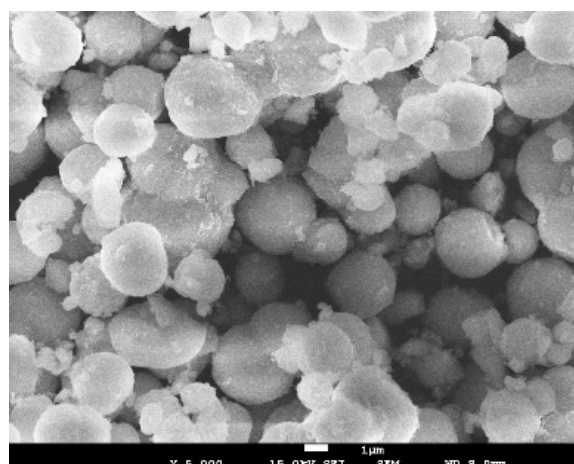

(**a**)   (**b**)

Figure 2. Crystal structure of (**a**) monoclinic Li_2MnO_3 structure with space group C2/m and (**b**) rhombohedral $LiMO_2$ structure. M = Ni, Mn with space group R3m using VESTA software.
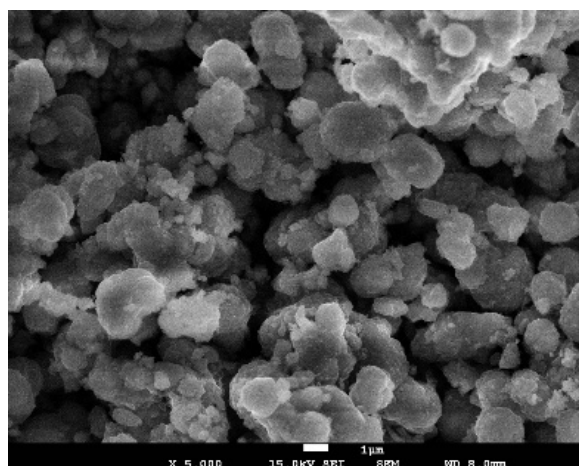

(**a**)   (**b**)

Figure 3. *Cont*.

Figure 3. SEM micrographs of (**a**) $Ni_{0.35}Mn_{0.65}CO_3$, (**b**) $Ni_{0.25}Mn_{0.75}CO_3$, and (**c**) $Ni_{0.15}Mn_{0.85}CO_3$ powders, the results of the first step of the synthesis process.

Figure 4. EDS spectra of (**a**) $Ni_{0.35}Mn_{0.65}CO_3$, (**b**) $Ni_{0.25}Mn_{0.75}CO_3$, and (**c**) $Ni_{0.15}Mn_{0.85}CO_3$ powders, the results of the first step of the synthesis process.
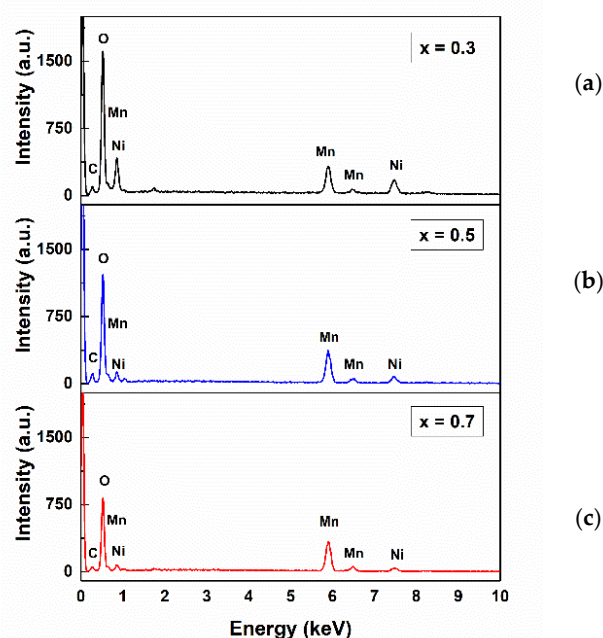
Micrographs of the synthesized $0.3Li_2MnO_3–0.7LiNi_{0.5}Mn_{0.5}O_2$, $0.5Li_2MnO_3–0.5LiNi_{0.5}Mn_{0.5}O_2$, and $0.7Li_2MnO_3–0.3LiNi_{0.5}Mn_{0.5}O_2$ final powders after calcination of precursors with Li_2CO_3 are showed in Figure 5. The primary particles are micrometric in size and concentrated in irregularly polyhedral-shaped agglomerations. Relatively smaller primary particle agglomerates allow better charge–discharge capacity due to their higher trap density, which shortens lithium diffusion [39]. The pristine x = 0.5 material composite presented a lower density of agglomerations compared with the other synthesized material. The precursor spherical shape could be the reason why a better formation of the final product was possible, which may help improve the electrochemical performance. The size of these agglomerations increased with the increase of x. For x = 0.7 particles that exceeded a micrometer in length, the characteristics of the precursor seemed to influence the growth mechanism for the formation of the final material [37,40]. The micrographs also show free space between agglomerations, giving a high material porosity, which is good for the ions' and electrons' mobility [40–42].
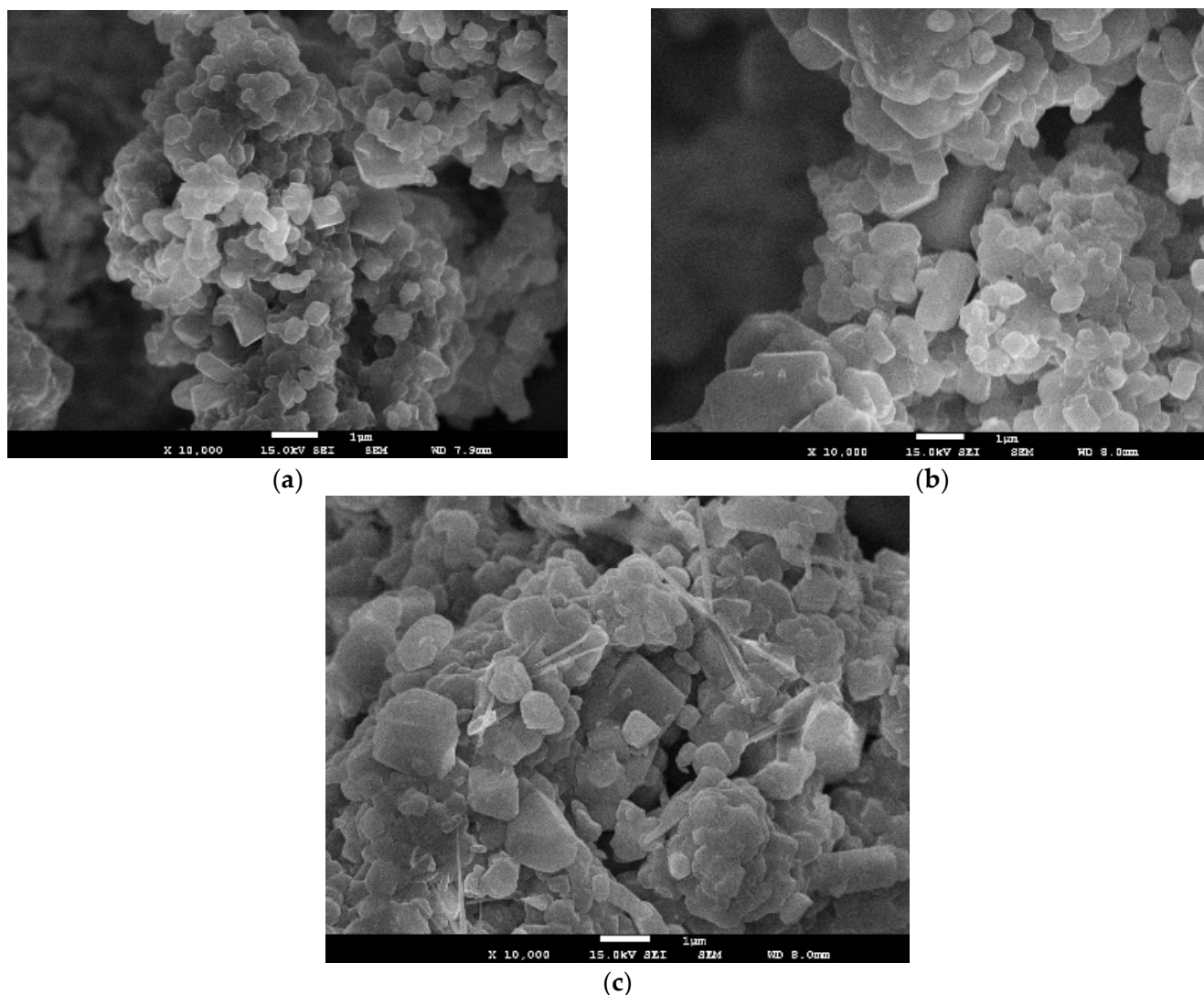
(**a**)

(**b**)

(**c**)

Figure 5. SEM micrographs of (**a**) $0.3Li_2MnO_3$–$0.7LiNi_{0.5}Mn_{0.5}O_2$, (**b**) $0.5Li_2MnO_3$–$0.5LiNi_{0.5}Mn_{0.5}O_2$, and (**c**) $0.7Li_2MnO_3$–$0.3LiNi_{0.5}Mn_{0.5}O_2$ cathode material powders.

The charge–discharge profiles and differential capacities for the 1st, 5th, 10th, and 40th cycles at a current density of 15 mA/g for (a) $0.3Li_2MnO_3$–$0.7LiNi_{0.5}Mn_{0.5}O_2$, (b) $0.5Li_2MnO_3$–$0.5LiNi_{0.5}Mn_{0.5}O_2$, and (c) $0.7Li_2MnO_3$–$0.3LiNi_{0.5}Mn_{0.5}O_2$ cathode material are shown in Figure 6. For the x = 0.3 electrode material (Figure 6(a1)), a clear two-step reaction appeared at the first charge process. There was a plateau voltage between 4–4.5 V corresponding to the Li extraction from $LiMO_2$ component, reaching a capacity of 120 mAh/g. The Li extraction from the Li_2MnO_3 component started from ~4.5 V as was predicted, and the capacity contributed to the total capacity is 103 mAh/g [43]. A possible explanation of low capacity is the current density used. High current densities deliver lower capacities, as some literatures present [20,39,42], and a lower current density can make Li extraction more effective. One other possibility is the formation of some spinel phase among the structure of the electrode material; this option is enhanced by the change to some clearly spinel phase at 40th cycles seen in the discharge process at ~3 V [44,45]. The decrease of capacities at high cycle numbers could be explained by the change from layered to spinel phase transformation, due to the migration of transition metal ions to Li sites without much disarrangement of the main layered structure [44]. A differential capacity plot (Figure 6(a2)) showed two sharp oxidation peaks at 4.1 V and 4.6 V, corresponding to the first charge two-step reactions of the $LiMO_2$ and Li_2MnO_3 components, respectively. The second

peak represents the irreversible loss of capacity when Li was extracted in the form of Li_2O [46]. The first peak, which was shifted to ~3.8 V in the next cycles, corresponds to the Ni oxidation from Ni^{2+} to Ni^{4+}. The manganese-corresponding oxidation peaks were not even visible in the 40th cycle. In the reduction zone, the predominant peak is around 3.8 V; this peak is associated with Ni reduction from Ni^{4+} to Ni^{2+}. At 40 cycles, a new peak arose at ~2.93 V, supporting the idea of some spinel phase formation. This peak is a characteristic peak of Mn reduction from Mn^{4+} to Mn^{3+} in the spinel structure [47].
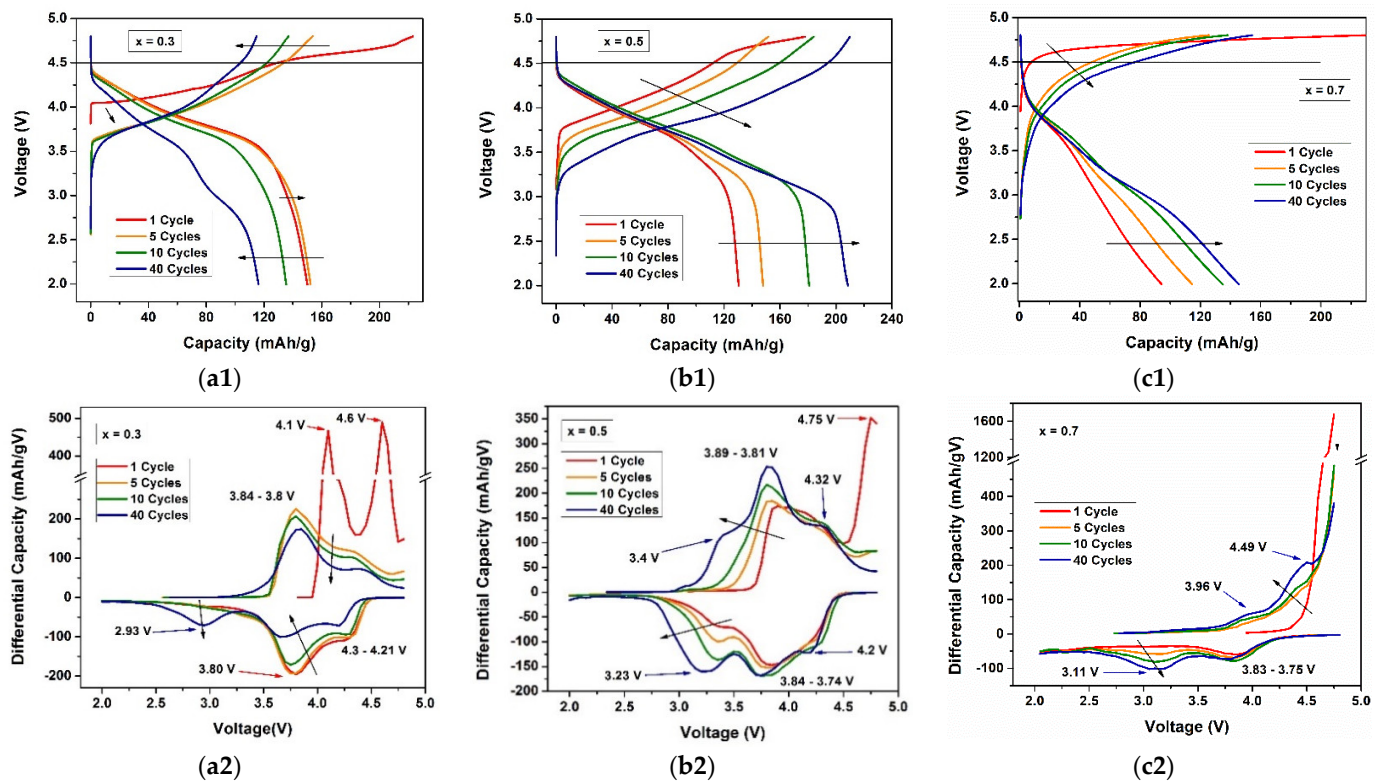

Figure 6. Charge–discharge profiles (**a1**–**c1**) and differential capacity plots (**a2**–**c2**) for the 1st, 5th, 10th, and 40th cycles for (**a**) $0.3Li_2MnO_3$–$0.7LiNi_{0.5}Mn_{0.5}O_2$, (**b**) $0.5Li_2MnO_3$–$0.5LiNi_{0.5}Mn_{0.5}O_2$, and (**c**) $0.7Li_2MnO_3$–$0.3LiNi_{0.5}Mn_{0.5}O_2$ cathode materials.

For the x = 0.5 electrode material (Figure 6(b1)), a two-step reaction also appeared for the first charge process. In the first step (2–4.5 V) related to the Li extraction from $LiMO_2$, a capacity of 123 mAh/g was achieved near the theoretical value for the charge capacity for this component. In the second step (4.5 V), a capacity of 55 mAh/g was delivered due to the activation of Li_2MnO_3 component. This value was significantly small compared with the theoretical value, revealing that not all Li_2MnO_3 material could be activated at this current density. Li_2MnO_3 shows to be electrochemically inactive before 4.5 V vs. Li/Li^+, because manganese has a 4^+ oxidation state, making the Li^+ intercalation difficult [35,47]. Electrochemical activity at a higher voltage is associated with the loss of oxygen by removing Li_2O, allowing a change in the phase to MnO_2 [48,49]. The first discharge capacity was 130 mAh/g, even lower when compared to the theoretical value, but still in the range of values reported in the literature [35,39]. Despite that, the capacity progressively increased through the cycles, achieving a regular capacity of around 210 mAh/g for the 40th cycle, showing the progressive activation of Li_2MnO_3 component. This was near the value of others obtained experimentally in some of the literature [35,37,39]. The differential capacity plot (Figure 6(b2)) showed a peak associated with the initial activation of Li_2MnO_3, which appeared around 4.75 V. Both the peaks of oxidation and reduction related to Ni and Mn reactions were present. The Ni oxidation from Ni^{2+} to Ni^{4+} was associated with the peak placed at ~3.81 V in the first cycle, which stabilized at

~3.89 V, indicating an increasing of activated Ni step-by-step during cycling. Similarly, Mn oxidation increased from Mn^{3+} to Mn^{4+}, as represented by the raised peak at 3.4 V. The reductions occurred at the potentials of ~3.84 for the Ni reduction and at the raised peak at ~3.23 V for the Mn reduction. A greater progressive activation of Mn was observed, more than that of Ni, confirming the idea of the step-by-step Li_2MnO_3 activation through cycling [40,47,50,51]. For the x = 0.7 electrode material (Figure 6(c1)), only one reaction was observed for the first charge process, related to the Li extraction from $LiMO_2$. It was not possible to observe the activation of the Li_2MnO_3 layer in the first cycle. For the following cycles, an increase in the discharge capacity was observed, until the capacity achieved 140 mAh/g in cycle 40. Li_2MnO_3 proved to be electrochemically inactive, possibly due to high impedance making the Li^+ intercalation difficult [49]. A differential capacity plot (Figure 6(c2)) showed the behavior of the first loading process, where it was not possible to observe peaks related to the complete activation of the material. After 10 cycles, peaks of oxidation and reduction related to Ni and Mn reactions appeared but shifted to the high voltage in the charge process and to the left in the discharge process, indicating the formation of spinel structures [45,52]. In all cases, the differential capacity values were very low, indicating an inefficient charge transfer process between the material and the electrolyte, possibly due to the size of the conglomerates that formed the material [32,39].

Figure 7 shows the charge–discharge profiles and differential capacity plots of the (a) $0.3Li_2MnO_3$–$0.7LiNi_{0.5}Mn_{0.5}O_2$, (b) $0.5Li_2MnO_3$–$0.5LiNi_{0.5}Mn_{0.5}O_2$, and (c) $0.7Li_2MnO_3$–$0.3LiNi_{0.5}Mn_{0.5}O_2$ cathode materials at different current densities of 15, 30, and 45 mA/g. The 20th cycle was taken for this analysis. For the x = 0.3 cathode material (Figure 7(a1)), the capacity was reduced from ~150 mAh/g (15 mA/g) to ~120 mAh/g (30 mA/g) and ~100 mAh/g (45 mA/g). An inflection point is shown between 3.5 and 4 V in the discharge process, where the capacity dropped drastically. A cathode material with x = 0.5 showed similar behavior (Figure 7(b1)) but reached higher capacities, i.e., ~210 mAh/g (15 mA/g), ~190 mAh/g (30 mA/g), and ~170 mAh/g (45 mA/g). For the x = 0.7 cathode materials, only one activation process was seen (Figure 7(c1)). The capacities achieved were ~140 mAh/g (15 mA/g), ~64 mAh/g (30 mA/g), and ~57 mAh/g (45 mA/g). The differential capacities of the cathode materials showed all peaks decreasing their intensities with the increase of the current density; additionally, a degradation of the voltage occurred when the current density increased [53,54]. These reductions of electrochemical performance could be explained by considering that, at high current densities, the amount of lithium insertion/extraction is affected due to the structure's surface not allowing to Li ions to leave their sites, resulting in low capacities [46]. For example, for x = 0.5 (Figure 7(b2)), the Mn oxidation from M^{3+} to Mn^{4+} at ~3.4 V was only seen at 15 mA/g and not at 45 mA/g. As we observed, for the lithium extraction process of xLi_2MnO_3–$(1-x)LiNi_{0.5}Mn_{0.5}O_2$, the charging process was carried out in two different steps. The first one was when lithium was extracted from the $LiMO_2$ component, typically at potentials < 4.5 V, accompanied by the oxidation of the M cations. A total of $(1-x)Li$ were removed from the $LiMO_2$ irreversible component to form MnO_2. The second step was the extraction of lithium from the Li_2MnO_3 component at potentials > 4.5 V. In this last step, oxygen was also extracted from the structure, giving a net loss of Li_2O. Next, xLi was extracted from the Li_2MnO_3 component to form MnO_2 [39,48,49]. In both reactions, the total lithium extracted rose to $(1+x)Li$. In the discharge process, lithium was reinserted into the structure. $(1-x)Li$ was reinserted into the MO_2 component, recovering the $LiMO_2$ initial component, but on the other hand, only xLi was reinserted into the MnO_2 component, resulting in $LiMnO_2$ with rock salt [48,49]. This was caused by its inability to reinsert oxygen into the structure during the discharge process, which means there must always be an irreversible capacity loss of xLi in the first cycle [40].
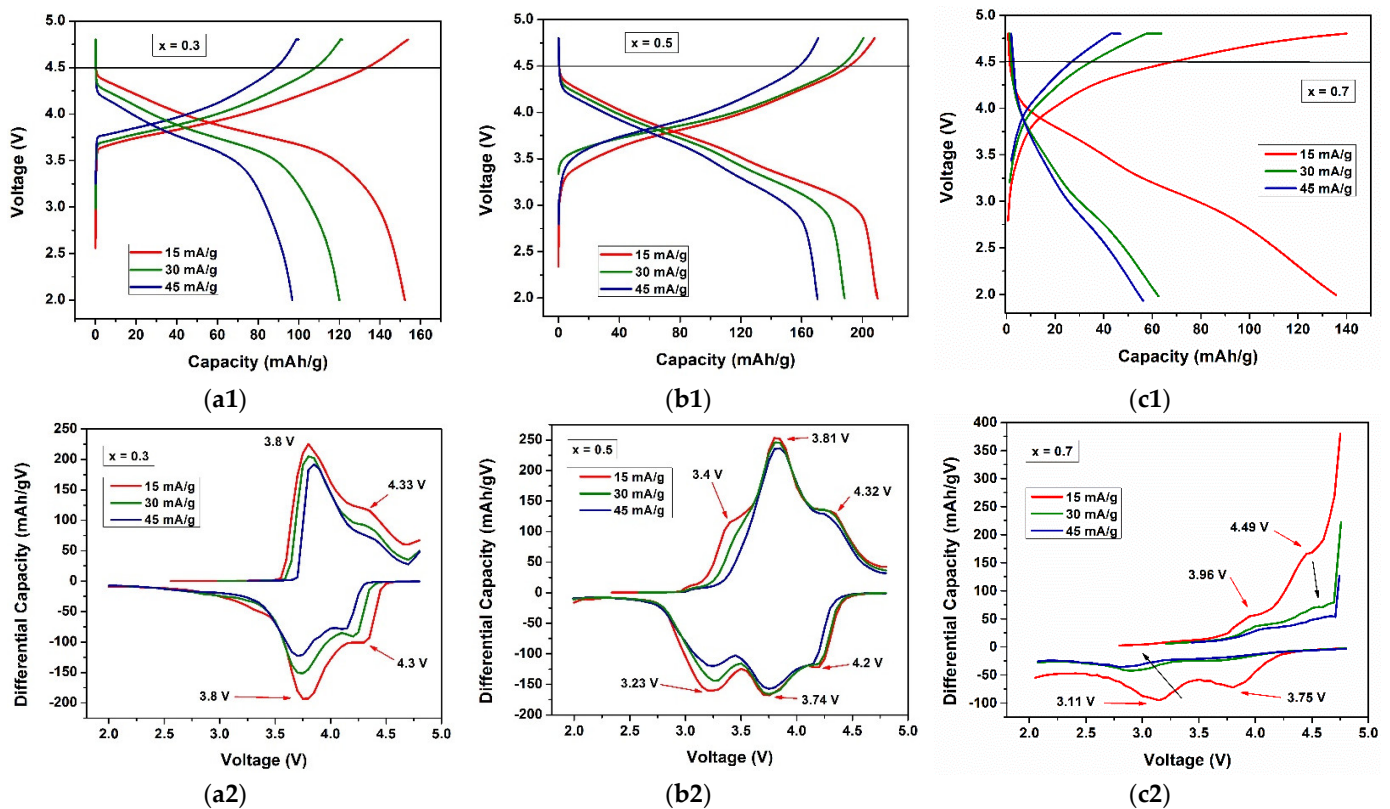
Figure 7. Charge–discharge profiles (**a1**–**c1**) and differential capacity plots (**a2**–**c2**) for 15, 30, and 45 mA/g current density for (**a**) $0.3Li_2MnO_3$–$0.7LiNi_{0.5}Mn_{0.5}O_2$, (**b**) $0.5Li_2MnO_3$–$0.5LiNi_{0.5}Mn_{0.5}O_2$, and (**c**) $0.7Li_2MnO_3$–$0.3LiNi_{0.5}Mn_{0.5}O_2$ cathode materials.

The variations of the charge–discharge capacity and coulombic efficiency through cycling for the (a) $0.3Li_2MnO_3$–$0.7LiNi_{0.5}Mn_{0.5}O_2$, (b) $0.5Li_2MnO_3$–$0.5LiNi_{0.5}Mn_{0.5}O_2$, and (c) $0.7Li_2MnO_3$–$0.3LiNi_{0.5}Mn_{0.5}O_2$ cathode materials are shown in Figure 8. For the x = 0.3 (Figure 8a) first cycle, the irreversible process was measured at a coulombic efficiency of around 68%. The discharge capacity was almost constant for the first 10 cycles, with a slight decrease in the last cycles, using a current density of 15 mA/g, although certain stability was also observed at higher current densities. For x = 0.5 (Figure 8b), the first-cycle charge–discharge capacities difference produced a higher coulombic efficiency of 73%. In this material, the discharge capacity using 15 mA/g gradually increased through cycling until the capacity was almost 220 mAh/g in the 19th cycle. This could be caused by an incomplete activation of the cathode material, or it may be due to the size of the particle and the long diffusion distance of Li+, which made it more difficult to activate them. A decrease in the next cycle to 210 mAh/g was then observed, remaining almost constant at this value. This is shown in Figure 6(b1), where at first charge the Li_2MnO_3 layer was not activated at all but activated slowly and continuously in the following cycles. This behavior is completely different compared with x = 0.3 (Figure 8a), which showed decreasing capacity, because the plateau seen on Figure 6(a1) was longer with a more complete activation of Li_2MnO_3, representing an irreversible loss [51]. For x = 0.7 (Figure 8c), the first-cycle charge–discharge capacities difference produced a low coulombic efficiency, around 20%. The cycling was almost constant at any current density but had low capacity. At the current densities of 30 and 45 mA/g, there was no significant difference, perhaps because of the high content of Li_2MnO_3 associated with cycling performance deterioration and its disposition to change structure to spinel form [40]. Additionally, it seemed that a low reversible capacity was possible due to a longer diffusion distance, which led to a slower rate of diffusion than was reflected in lower capacities, as seen in this study [55].
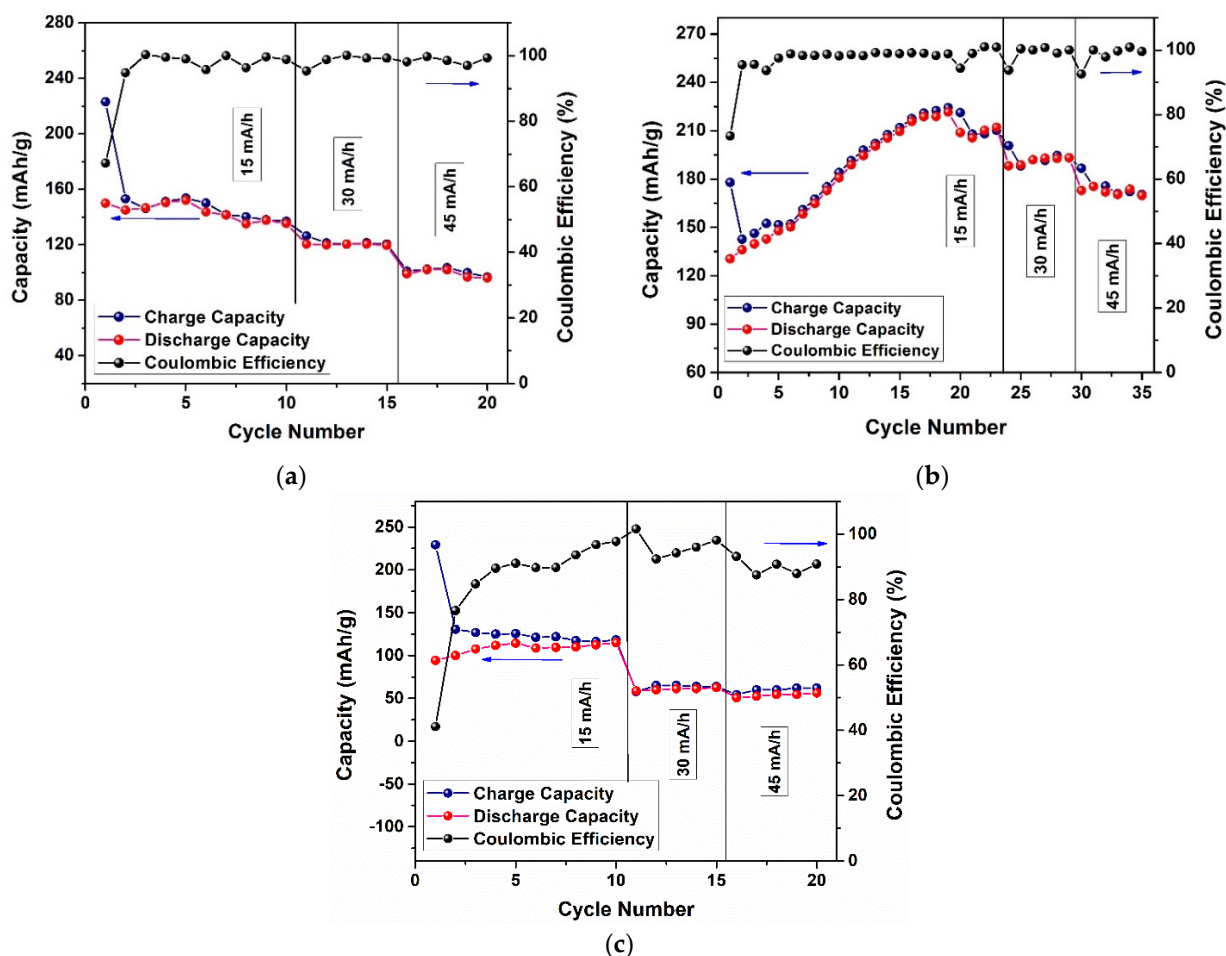
Figure 8. Charge–discharge capacity and coulombic efficiency through cycling for (**a**) $0.3Li_2MnO_3$–$0.7LiNi_{0.5}Mn_{0.5}O_2$, (**b**) $0.5Li_2MnO_3$–$0.5LiNi_{0.5}Mn_{0.5}O_2$, and (**c**) $0.7Li_2MnO_3$–$0.3LiNi_{0.5}Mn_{0.5}O_2$ cathode materials.

Electrochemical impedance spectroscopy (EIS) measurements were carried out on the electrochemical cells prepared with the synthesized materials, and the Nyquist plot results are shown in Figure 9. EIS allows us to understand the various situations that occur at the interface of the electrode and the electrolyte through a non-destructive technique that determines the impedance of the electrochemical cell based on small AC signals, with constant DC voltages in a wide range of frequencies [56]. The impedance spectra were obtained within the frequency range of 10 mHz to 100 kHz. Each EIS spectrum presented two overlapped semicircles due to the combination of a capacitor and a resistor element connected in parallel and an inclined line in the low-frequency region. This characteristic plot suggested the contribution of two different resistive elements to the total impedance of the cell. The high-frequency semicircle represents the impedance of the surface electrolyte interface (SEI) film (R_{sf}), the medium frequency semicircle denotes the charge transfer impedance across the interface (R_{ct}), and the small interrupt in the high frequency corresponds to the electrolyte impedance (R_e) [29,40]. All parameters were represented by plot fitting, with the electrochemical equivalent circuit (EEC) shown on Figure 10. Where CPE_1 represents the capacitance of SEI film, which grows thicker by electrolyte–electrode reaction during charge–discharge and deteriorates the performance, CPE_2 corresponds to charge–transfer capacitance, and Z_w is the Warburg impedance related to the lithium ions' diffusion. The impedance parameters' (R_{sf}, R_{ct} and R_e) values after fitting are summarized in Table 1.
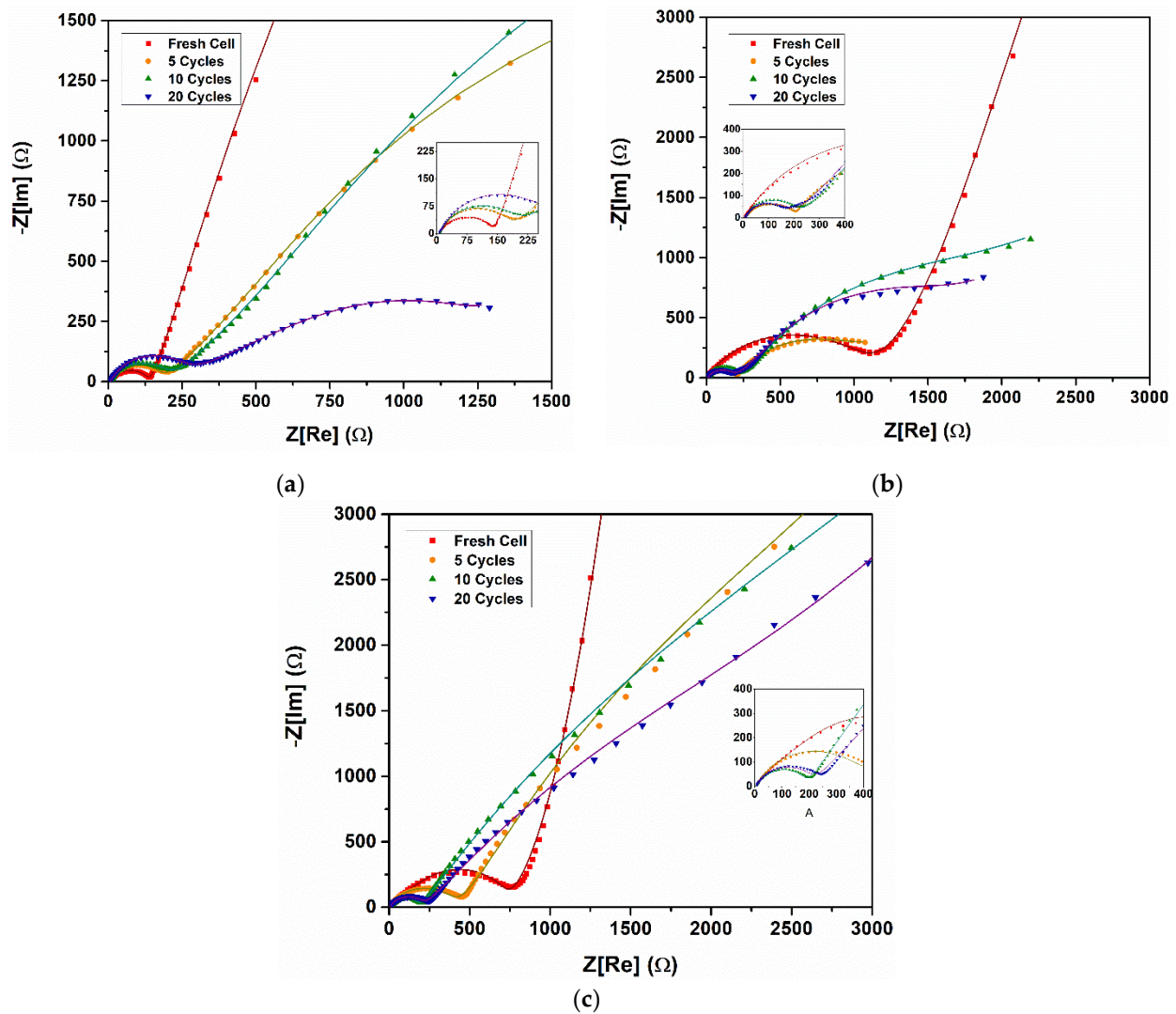
Figure 9. Impedance spectrum of the (**a**) $0.3Li_2MnO_3$–$0.7LiNi_{0.5}Mn_{0.5}O_2$, (**b**) $0.5Li_2MnO_3$–$0.5LiNi_{0.5}Mn_{0.5}O_2$, and (**c**) $0.7Li_2MnO_3$–$0.3LiNi_{0.5}Mn_{0.5}O_2$ cathode materials.
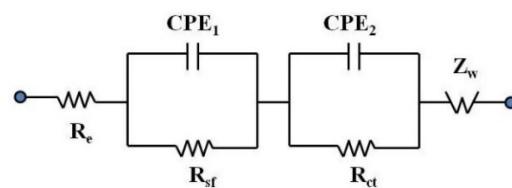

Figure 10. Electrochemical electric circuit (EEC) used to fit the EIS data.

For electrochemical cells with the x = 0.3 layered material (Figure 9a), an increase in the area of semicircle was observed as the number of cycles increased. An increase in the R_{sf} was expected because of the growth of the SEI layer at the interface of the electrolyte and electrode surface; nevertheless, a high resistance value was found at the first cycle, as shown in Table 2. This can explain the late activation of the $LiMO_2$-associated layer around 4 V. For subsequent cycles, the impedance was drastically reduced to 900 Ω to increase when reaching 20 cycles. In the other hand, the R_{ct} impedance increased with cycles; this behavior could explain the decrease in discharge capacity observed in Figure 6a and poor cycling stability [57]. Electrochemical cells with x = 0.5 (Figure 9b) showed a large reduction in semicircle diameter of the high-frequency region with the cycle increasing, related to a reduction of the charge–transfer resistance, which could be beneficial for improving the

discharge capacity [25]. A large difference in diameter between the first cycle and the following was clearly seen. For the fifth, tenth, and twentieth, diameter was highly similar, revealing that the SEI film formed mostly during the first charge–discharge process and remained stable during the following charge–discharge cycles. Additionally, since the R_{ct} value decreased during large cycles, with this material it is possible to reach high capacity values, as well as the composite layer structure becoming more stable, which improves cyclability during the charge–discharge process, as shown in Figure 8b. Finally, for the cells with x = 0.7, although the diameters of the semicircles in the high frequency region had a behavior similar to that analyzed above, they did not present the second semicircle in the low frequency region. Instead, almost straight "tails" were observed (Figure 9c). Since the first cycle was a very inclined one and exceeded 45°, this was associated with the large size of the particles [40], which could explain the low capacity reached in the electrochemical cells using this material.

Table 2. Impedance parameters obtained after fitting the EIS experimental data based on the EEC model shown in Figure 9.

Impedance Parameter	x\Cycle	1st	5th	10th	20th
R_{sf} (Ω)	0.3	14,760	900	900	1067
	0.5	505.4	81.03	65.37	2087
	0.7	435.1	2688	5000	1500
R_{ct} (Ω)	0.3	130	167.9	197.5	221.1
	0.5	0.9519	1758	965.9	66.63
	0.7	265.7	400	180	200
R_e (Ω)	0.3	7.901	7.217	7.539	3.273
	0.5	9.380	4.45	4.807	6.000
	0.7	4.408	7.501	1.532	5.699

4. Conclusions

In this study, a xLi_2MnO_3–$(1-x)LiNi_{0.5}Mn_{0.5}O_2$ layered composite material for x = 0.3, 0.5, and 0.7 was synthesized by a carbonate-assisted co-precipitation method. The X-ray diffraction patterns confirmed the formation of the two-phase layered crystal structure, the rhombohedral $LiMO_2$ structure with R3m space group, and the monoclinic Li_2MnO_3 structure with C2/m space group. We also observed a decrease in the size of the lattice parameters with the decrease in the amount of Ni. The CR2032 coin cells were successfully assembled in an Ar-filled glove box in order to test the electrochemical behavior of the synthesized electrode materials. The electrochemical results show the two-step Li extraction, one at potential <4.5 V related to the Li extraction from $LiMO_2$, and the other at potential >4.5, which corresponds to the activation of Li_2MnO_3 by means of the extraction of Li in the form of LiO_2. As x increased, the charge and discharge reactions assigned to the component similar to Li_2MnO_3 increased, while those corresponding to $LiMO_2$ decreased, producing an activation that allowed high capacities to be reached. However, there was a limit related to the size of the particle agglomerates and some spinel phase formation within the structure of the first material, which was reflected in a slow diffusion rate, inefficient Li_2MnO_3 activation, and low capacities. Better electrochemical performance was found for the x = 0.5 electrode material with a first-charge capacity of 173 mAh/g and a higher discharge capacity of 210 mAh/g.

Author Contributions: Conceptualization, R.N.-N.; methodology, R.N.-N., S.R.-F. and L.J.-C.; software, M.G.-C. and F.N.D.; validation, R.N.-N., L.A.-S. and S.M.B.; formal analysis, R.N.-N.; investigation, R.N.-N. and L.J.-C.; data curation, M.G.-C. and F.N.D.; writing—original draft preparation, R.N.-N.; writing—review and editing, S.R.-F. and M.G.-C.; project administration, R.N.-N. and S.M.B. All authors have read and agreed to the published version of the manuscript.

References

1.　Ghosh, S.; Bhattacharjee, U.; Bhowmik, S.; Martha, D.; Surendra, K. A Review on High-Capacity and High-Voltage Cathodes for Next-Generation Lithium-ion Batteries. *J. Energy Power Technol.* **2022**, *4*, 1–59. [CrossRef]

2.　Rojas-Flores, S.; Pérez-Delgado, O.; Nazario-Naveda, R.; Rojales-Alfaro, H.; Benites, S.M.; La Cruz-Noriega, D.; Otiniano, N.M. Potential Use of Papaya Waste as a Fuel for Bioelectricity Generation. *Processes* **2021**, *9*, 1799. [CrossRef]

3.　Segundo, R.F.; La Cruz-Noriega, D.; Milly Otiniano, N.; Benites, S.M.; Esparza, M.; Nazario-Naveda, R. Use of Onion Waste as Fuel for the Generation of Bioelectricity. *Molecules* **2022**, *27*, 625. [CrossRef] [PubMed]

4.　Nazario-Naveda, R.; Benites, S.M. Sugar Industry Waste for Bioelectricity Generation. Environ. *Res. Eng. Manag.* **2021**, *77*, 15–22. [CrossRef]

5.　Segundo, R.F.; Renny, N.N.; Moises, G.C.; Daniel, D.N.; Natalia, D.D.; Karen, V.R. Generation of Bioelectricity from Organic Fruit Waste. *Environ. Res. Eng. Manag.* **2021**, *77*, 6–14. [CrossRef]

6.　Hayner, C.M.; Zhao, X.; Kung, H.H. Materials for rechargeable lithium-ion batteries. *Annu. Rev. Chem. Biomol. Eng.* **2012**, *3*, 445–471. [CrossRef]

7.　Konishi, H.; Hirano, T.; Takamatsu, D.; Gunji, A.; Feng, X.; Furutsuki, S.; Takahashi, S.; Terada, S. Potential hysteresis between charge and discharge reactions in $Li_{1.2}Ni_{0.13}Mn_{0.54}Co_{0.13}O_2$ for lithium ion batteries. *Solid State Ion.* **2017**, *300*, 120–127. [CrossRef]

8.　Konishi, H.; Hirano, T.; Takamatsu, D.; Gunji, A.; Feng, X.; Furutsuki, S.; Okumura, T.; Terada, S.; Tamura, K. Mechanisms responsible for two possible electrochemical reactions in $Li_{1.2}Ni_{0.13}Mn_{0.54}Co_{0.13}O_2$ used for lithium ion batteries. *J. Solid State Chem.* **2018**, *258*, 225–231. [CrossRef]

9.　Luo, K.; Roberts, M.R.; Guerrini, N.; Tapia-Ruiz, N.; Hao, R.; Massel, F.; Pickup, D.M.; Ramos, S.; Liu, Y.S.; Guo, J.; et al. Anion redox chemistry in the cobalt free 3d transition metal oxide intercalation electrode $Li[Li_{0.2}Ni_{0.2}Mn_{0.6}]O_2$. *J. Am. Chem. Soc.* **2016**, *138*, 11211–11218. [CrossRef]

10.　Nisa, S.S.; Rahmawati, M.; Yudha, C.S.; Nilasary, H.; Nursukatmo, H.; Oktaviano, H.S.; Muzayanha, S.U.; Purwanto, A. A Fast Approach to Obtain Layered Transition-Metal Cathode Material for Rechargeable Batteries. *Batteries* **2022**, *8*, 4. [CrossRef]

11.　Klink, J.; Hebenbrock, A.; Grabow, J.; Orazov, N.; Nylén, U.; Benger, R.; Beck, H.-P. Comparison of Model-Based and Sensor-Based Detection of Thermal Runaway in Li-Ion Battery Modules for Automotive Application. *Batteries* **2022**, *8*, 34. [CrossRef]

12.　Xu, B.; Qian, D.; Wang, Z.; Meng, Y.S. Recent progress in cathode materials research for advanced lithium ion batteries. *Mater. Sci. Eng. R Rep.* **2012**, *73*, 51–65. [CrossRef]

13.　Yu, H.; Zhou, H. High-energy cathode materials (Li_2MnO_3–$LiMO_2$) for lithium-ion batteries. *J. Phys. Chem. Lett.* **2013**, *4*, 1268–1280. [CrossRef] [PubMed]

14.　Konishi, H.; Hirano, T.; Takamatsu, D.; Gunji, A.; Feng, X.; Furutsuki, S.; Okumura, T.; Terada, S. Suppression of potential hysteresis between charge and discharge reactions in lithium-rich layer-structured cathode material by increasing nickel/manganese ratio. *Solid State Ion.* **2017**, *308*, 84–89. [CrossRef]

15.　Hou, X.; Wang, Y.; Song, J.; Gu, H.; Guo, R.; Liu, W.; Mao, Y.; Xie, J. Electrochemical behavior of Mn-based Li-rich cathode material $Li_{1.15}Ni_{0.17}Co_{0.11}Mn_{0.57}O_2$ fluorinated by NH4F. *Solid State Ion.* **2018**, *325*, 1–6. [CrossRef]

16.　Li, Y.C.; Xiang, W.; Wu, Z.G.; Xu, C.L.; Xu, Y.D.; Xiao, Y.; Yang, Z.G.; Wu, C.J.; Lv, G.P.; Guo, X.D. Construction of homogeneously Al^{3+} doped Ni rich Ni-Co-Mn cathode with high stable cycling performance and storage stability via scalable continuous precipitation. *Electrochim. Acta* **2018**, *291*, 84–94. [CrossRef]

17.　Wang, C.C.; Lin, Y.C.; Chiu, K.F. Alleviation of voltage fade of lithium-rich layered oxide cathodes of Li-ion battery by incorporation of Cr. *J. Alloy. Compd.* **2017**, *721*, 600–608. [CrossRef]

18.　Zou, T.; Qi, W.; Liu, X.; Wu, X.; Fan, D.; Guo, S.; Wang, L. Improvement of the electrochemical performance of $Li_{1.2}Ni_{0.13}Co_{0.13}Mn_{0.54}O_2$ cathode material by Al_2O_3 surface coating. *J. Electroanal. Chem.* **2020**, *859*, 113845. [CrossRef]

19.　Zhong, J.; Yang, Z.; Yu, Y.; Liu, Y.; Li, J.; Kang, F. Surface substitution of polyanion to improve structure stability and electrochemical properties of lithium-rich layered cathode oxides. *Appl. Surf. Sci.* **2020**, *512*, 145741. [CrossRef]

20.　Kim, D.; Sandi, G.; Croy, J.R.; Gallagher, K.G.; Kang, S.H.; Lee, E.; Slater, M.D.; Johnson, C.S.; Thackeray, M.M. Composite layered-layered-spinel cathode structures for lithium-ion batteries. *J. Electrochem. Soc.* **2012**, *160*, A31. [CrossRef]

21.　Xiao, L.; Xiao, J.; Yu, X.; Yan, P.; Zheng, J.; Engelhard, M.; Bhattacharya, P.; Wang, C.; Yang, X.Q.; Zhang, J.G. Effects of structural defects on the electrochemical activation of $Li2MnO3$. *Nano Energy* **2015**, *16*, 143–151. [CrossRef]

22.　Zhang, K.; Li, B.; Zuo, Y.; Song, J.; Shang, H.; Ning, F.; Xia, D. Voltage decay in layered Li-rich Mn-based cathode materials. *Electrochem. Energy Rev.* **2019**, *2*, 606–623. [CrossRef]

23.　Baggetto, L.; Dudney, N.J.; Veith, G.M. Surface chemistry of metal oxide coated lithium manganese nickel oxide thin film cathodes studied by XPS. *Electrochim. Acta* **2013**, *90*, 135–147. [CrossRef]

24.　Zhou, D.; Liu, R.; He, Y.B.; Li, F.; Liu, M.; Li, B.; Yang, Q.H.; Cai, Q.; Kang, F. SiO_2 hollow nanosphere-based composite solid electrolyte for lithium metal batteries to suppress lithium dendrite growth and enhance cycle life. *Adv. Energy Mater.* **2016**, *6*, 1502214. [CrossRef]

25. Shojan, J.; Chitturi, V.R.; Torres, L.; Singh, G.; Katiyar, R.S. Lithium-ion battery performance of layered 0.3Li$_2$MnO$_3$–0.7LiNi$_{0.5}$Mn$_{0.5}$O$_2$ composite cathode prepared by co-precipitation and sol–gel methods. *Mater. Lett.* **2013**, *104*, 57–60. [CrossRef]

26. Xiang, Y.; Jiang, Y.; Liu, S.; Wu, J.; Liu, Z.; Zhu, L.; Xiong, L.; He, Z.; Wu, X. Improved electrochemical performance of 0.5Li$_2$MnO$_3$-0.5LiNi$_{0.5}$Mn$_{0.5}$O$_2$ cathode materials for lithium ion batteries synthesized by ionic-liquid-assisted hydrothermal method. *Front. Chem.* **2020**, *8*, 729. [CrossRef]

27. Bettge, M.; Li, Y.; Sankaran, B.; Rago, N.D.; Spila, T.; Haasch, R.T.; Petrov, I.; Abraham, D.P. Improving high-capacity Li$_{1.2}$Ni$_{0.15}$Mn$_{0.55}$Co$_{0.1}$O$_2$-based lithium-ion cells by modifiying the positive electrode with alumina. *J. Power Sources* **2013**, *233*, 346–357. [CrossRef]

28. Klein, A.; Axmann, P.; Yada, C.; Wohlfahrt-Mehrens, M. Improving the cycling stability of Li$_2$MnO$_3$ by surface treatment. *J. Power Sources* **2015**, *288*, 302–307. [CrossRef]

29. Lin, J.; Mu, D.; Jin, Y.; Wu, B.; Ma, Y.; Wu, F. Li-rich layered composite Li[Li$_{0.2}$Ni$_{0.2}$Mn$_{0.6}$]O$_2$ synthesized by a novel approach as cathode material for lithium ion battery. *J. Power Sources* **2013**, *230*, 76–80. [CrossRef]

30. Wu, Q.; Zhang, X.; Sun, S.; Wan, N.; Pan, D.; Bai, Y.; Zhu, H.; Hu, Y.S.; Dai, S. Improved electrochemical performance of spinel LiMn$_{1.5}$Ni$_{0.5}$O$_4$ through MgF$_2$ nano-coating. *Nanoscale* **2015**, *7*, 15609–15617. [CrossRef]

31. Song, L.; Tang, Z.; Chen, Y.; Xiao, Z.; Li, L.; Zheng, H.; Li, B.; Liu, Z. Structural analysis of layered Li$_2$MnO$_3$–LiMO$_2$ (M= Ni$_{1/3}$Mn$_{1/3}$Co$_{1/3}$, Ni$_{1/2}$Mn$_{1/2}$) cathode materials by Rietveld refinement and first-principles calculations. *Ceram. Int.* **2016**, *42*, 8537–8544. [CrossRef]

32. Redel, K.; Kulka, A.; Plewa, A.; Molenda, J. High-performance Li-rich layered transition metal oxide cathode materials for Li-ion batteries. *J. Electrochem. Soc.* **2019**, *166*, A5333. [CrossRef]

33. Gabrielli, G.; Marinaro, M.; Mancini, M.; Axmann, P.; Wohlfahrt-Mehrens, M. A new approach for compensating the irreversible capacity loss of high-energy Si/C | LiNi$_{0.5}$Mn$_{1.5}$O$_4$ lithium-ion batteries. *J. Power Sources* **2017**, *351*, 35–44. [CrossRef]

34. Hua, W.; Chen, M.; Schwarz, B.; Knapp, M.; Bruns, M.; Barthel, J.; Yang, X.; Sigel, F.; Azmi, R.; Senyshyn, A.; et al. Lithium/Oxygen Incorporation and Microstructural Evolution during Synthesis of Li-Rich Layered Li[Li$_{0.2}$Ni$_{0.2}$Mn$_{0.6}$]O$_2$ Oxides. *Adv. Energy Mater.* **2019**, *9*, 1803094. [CrossRef]

35. Konishi, H.; Hirano, T.; Takamatsu, D.; Okumura, T. Electrochemical reaction mechanism of two components in xLi$_2$MnO$_3$–(1–x)LiNi$_{0.5}$Mn$_{0.5}$O$_2$ and effect of x on the electrochemical performance in lithium ion battery. *J. Electroanal. Chem.* **2020**, *873*, 114402. [CrossRef]

36. Jiang, Y.; Yang, Z.; Luo, W.; Hu, X.; Huang, Y. Hollow 0.3Li$_2$MnO$_3$-0.7LiNi$_{0.5}$Mn$_{0.5}$O$_2$ microspheres as a high-performance cathode material for lithium–ion batteries. *Phys. Chem. Chem. Phys.* **2013**, *15*, 2954–2960. [CrossRef] [PubMed]

37. Xiang, Y.; Li, J.; Liao, Q.; Wu, X. Morphology and particle growth of Mn-based carbonate precursor in the presence of ethylene glycol for high-capacity Li-rich cathode materials. *Ionics* **2019**, *25*, 81–87. [CrossRef]

38. Guo, J.; Deng, Z.; Yan, S.; Lang, Y.; Gong, J.; Wang, L.; Liang, G. Preparation and electrochemical performance of LiNi0. 5Mn1. 5O4 spinels with different particle sizes and surface orientations as cathode materials for lithium-ion battery. *J. Mater. Sci.* **2020**, *55*, 13157–13176. [CrossRef]

39. Singh, G.; West, W.C.; Soler, J.; Katiyar, R.S. In situ Raman spectroscopy of layered solid solution Li$_2$MnO$_3$–LiMO$_2$ (M = Ni, Mn, Co). *J. Power Sources* **2012**, *218*, 34–38. [CrossRef]

40. Liu, C.; Wu, M.; Zong, Y.; Zhang, L.; Yang, Y.; Yang, G. Synthesis and structural properties of xLi$_2$MnO$_3$-(1-x)LiNi$_{0.5}$Mn$_{0.5}$O$_2$ single crystals towards enhancing reversibility for lithium-ion battery/pouch cells. *J. Alloy. Compd.* **2019**, *770*, 490–499. [CrossRef]

41. Xiang, Y.; Sun, Z.; Li, J.; Wu, X.; Liu, Z.; Xiong, L.; Yin, Z. Improved electrochemical performance of Li$_{1.2}$Ni$_{0.2}$Mn$_{0.6}$O$_2$ cathode material for lithium ion batteries synthesized by the polyvinyl alcohol assisted sol-gel method. *Ceram. Int.* **2017**, *43*, 2320–2324. [CrossRef]

42. Yu, C.; Li, G.; Guan, X.; Zheng, J.; Li, L. Composites Li$_{1+x}$Mn$_{0.5+0.5\ x}$Ni$_{0.5−0.5x}$O$_2$ (0.1 ≤ x ≤ 0.4): Optimized preparation to yield an excellent cycling performance as cathode for lithium-ion batteries. *Electrochim. Acta* **2012**, *61*, 216–224. [CrossRef]

43. Wang, J.; He, X.; Paillard, E.; Laszczynski, N.; Li, J.; Passerini, S. Lithium-and Manganese-Rich Oxide Cathode Materials for High-Energy Lithium Ion Batteries. *Adv. Energy Mater.* **2016**, *6*, 1600906. [CrossRef]

44. Gu, M.; Belharouak, I.; Zheng, J.; Wu, H.; Xiao, J.; Genc, A.; Amine, K.; Thevuthasan, S.; Baer, D.R.; Zhang, J.G.; et al. Formation of the spinel phase in the layered composite cathode used in Li-ion batteries. *ACS Nano* **2013**, *7*, 760–767. [CrossRef]

45. Hy, S.; Liu, H.; Zhang, M.; Qian, D.; Hwang, B.J.; Meng, Y.S. Performance and design considerations for lithium excess layered oxide positive electrode materials for lithium ion batteries. *Energy Environ. Sci.* **2016**, *9*, 1931–1954. [CrossRef]

46. Hy, S.; Felix, F.; Rick, J.; Su, W.N.; Hwang, B.J. Direct In situ observation of Li$_2$O evolution on Li-Rich high-capacity cathode material, Li[Ni$_x$Li$_{(1−2x)/3}$Mn$_{(2−x)/3}$]O$_2$ (0 ≤ x ≤ 0.5). *J. Am. Chem. Soc.* **2014**, *136*, 999–1007. [CrossRef]

47. Buzlukov, A.; Mouesca, J.M.; Buannic, L.; Hediger, S.; Simonin, L.; Canevet, E.; Colin, J.F.; Gutel, T.; Bardet, M. Li-Rich Mn/Ni Layered Oxide as Electrode Material for Lithium Batteries: A 7Li MAS NMR Study Revealing Segregation into (Nanoscale) Domains with Highly Different Electrochemical Behaviors. *J. Phys. Chem. C* **2016**, *120*, 19049–19063. [CrossRef]

48. Oishi, M.; Yogi, C.; Watanabe, I.; Ohta, T.; Orikasa, Y.; Uchimoto, Y.; Ogumi, Z. Direct observation of reversible charge compensation by oxygen ion in Li-rich manganese layered oxide positive electrode material, Li$_{1.16}$Ni$_{0.15}$Co$_{0.19}$Mn$_{0.50}$O$_2$. *J. Power Sources* **2015**, *276*, 89–94. [CrossRef]

49. Zhao, S.; Yan, K.; Zhang, J.; Sun, B.; Wang, G. Reaction Mechanisms of Layered Lithium-Rich Cathode Materials for High-Energy Lithium-Ion Batteries. *Angew. Chem. Int. Ed.* **2021**, *60*, 2208–2220. [CrossRef]

50. Yang, P.; Li, H.; Wei, X.; Zhang, S.; Xing, Y. Structure tuned $Li_{1.2}Mn_{0.6}Ni_{0.2}O_2$ with low cation mixing and Ni segregation as high-performance cathode materials for Li-ion batteries. *Electrochim. Acta* **2018**, *271*, 276–283. [CrossRef]

51. Hy, S.; Su, W.N.; Chen, J.M.; Hwang, B.J. Soft X-ray absorption spectroscopic and Raman studies on Li1. 2Ni0. 2Mn0. 6O2 for lithium-ion batteries. *J. Phys. Chem. C* **2012**, *116*, 25242–25247. [CrossRef]

52. Peng, H.; Zhao, S.X.; Huang, C.; Yu, L.Q.; Fang, Z.Q.; Wei, G.D. In Situ construction of spinel coating on the surface of a lithium-rich manganese-based single crystal for inhibiting voltage fade. *ACS Appl. Mater. Interfaces* **2020**, *12*, 11579–11588. [CrossRef] [PubMed]

53. Konishi, H.; Gunji, A.; Feng, X.; Furutsuki, S. Effect of transition metal composition on electrochemical performance of nickel-manganese-based lithium-rich layer-structured cathode materials in lithium-ion batteries. *J. Solid State Chem.* **2017**, *249*, 80–86. [CrossRef]

54. Konishi, H.; Terada, S.; Okumura, T. Effect of Lithium/Transition-Metal Ratio on the Electrochemical Properties of Lithium-Rich Cathode Materials with Different Nickel/Manganese Ratios for Lithium-Ion Batteries. *ChemistrySelect* **2019**, *4*, 9444–9450. [CrossRef]

55. Yang, F.; Zhang, Q.; Hu, X.; Peng, T. Synthesis of layered $xLi_2MnO_3 \cdot (1-x)LiMnO_2$ nanoplates and its electrochemical performance as Li-rich cathode materials for Li-ion battery. *Electrochim. Acta* **2015**, *165*, 182–190. [CrossRef]

56. Meddings, N.; Heinrich, M.; Overney, F.; Lee, J.S.; Ruiz, V.; Napolitano, E.; Seitz, S.; Hinds, G.; Raccichini, R.; Gaberšček, M.; et al. Application of electrochemical impedance spectroscopy to commercial Li-ion cells: A review. *J. Power Sources* **2020**, *480*, 228742. [CrossRef]

57. Nie, Y.; Xiao, W.; Miao, C.; Xu, M.; Wang, C. Effect of calcining oxygen pressure gradient on properties of $LiNi_{0.8}Co_{0.15}Al_{0.05}O_2$ cathode materials for lithium ion batteries. *Electrochim. Acta* **2020**, *334*, 135654. [CrossRef]